**SCIENCE CHINA**
Information Sciences

• **Supplementary File** •

# Co-channel multiplexing for Rayleigh-scattering-based information systems

Anchi WAN[1], Yingqing WU[1], Shibo ZHANG[1], Zhenyu YE[1], Yongxin LIAGN[1], Siyuan PENG[1], Ke LIU[1], Ziwen DENG[1], Han WU[2] & Zinan WANG[1*]

[1]*Key Laboratory of Optical Fiber Sensing and Communications, University of Electronic Science and Technology of China, Chengdu 611731, China;*
[2]*School of Electronics and Information Engineering, Sichuan University, Chengdu, Sichuan 610064, China*

## Appendix A  Cause of inter-channel crosstalk in CCM-DAS

Inter-channel crosstalk (ICC) is a common issue in channel-multiplexed DAS. In channel-multiplexed DAS, $M$ groups of pulses are injected into the fiber within one repetition period of $T_{\rm rep}$, leading to the overlapping of RBS signals from different probe pulses. At the signal processing end, the signals from different probe pulses are isolated through correlation operations or pulse compression operations, interweaved according to the injection sequence, and then combined to obtain the ultimate sensing signal. Generally, to alleviate ICC caused by signal overlap, the frequency resources occupied by $M$ probe pulses are maintained independently of each other. This leads to reduced correlation among the corresponding RBS signals, thus lowering the interference level between these signals. Examples of such techniques include FDM-based DAS [1] and OFDM-based DAS [2]. However, these approaches would occupy multiple frequency bands, resulting in excessive consumption of frequency resources, and the number of reused channels is limited by the available system bandwidth. In contrast, the co-channel multiplexing technique proposed in this work resolves these issues by having $M$ probe pulses occupy only one frequency band. The primary challenge that needs to be overcome is the ICC between these same-frequency channels.

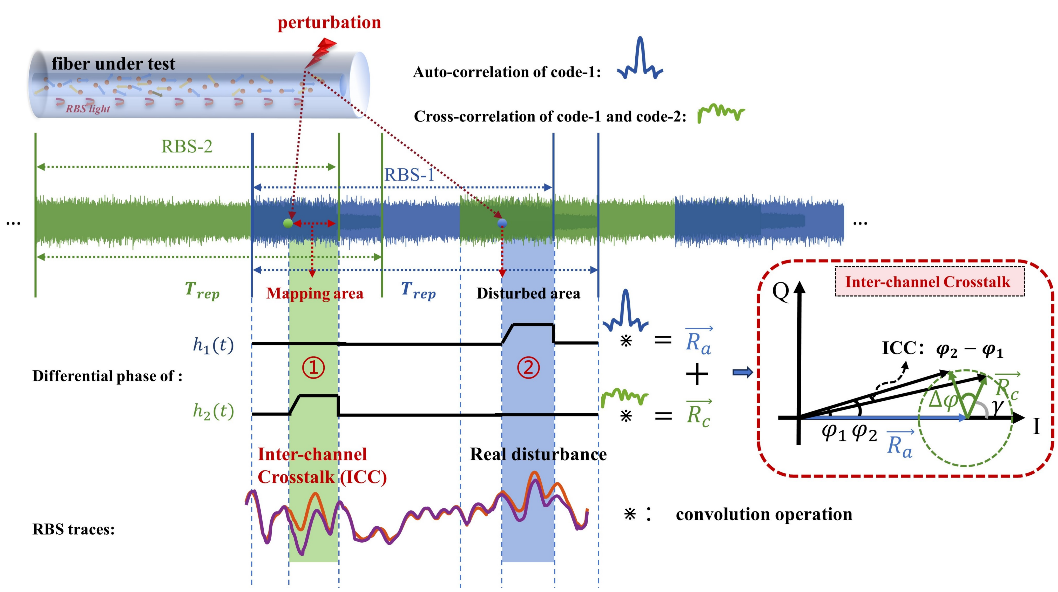


**Figure A1**  Schematic concept of the cause of the inter-channel crosstalk.

Figure A1 illustrates the origins of ICC in co-channel multiplexing through a two-channel example. It also details the strategies and principles for effectively mitigating ICC. Here, a coded pulse sequence with two sets of orthogonal codes is pumped into the fiber under test (FUT) within a repetition period of $T_{\rm rep}$, yielding two types of RBS traces denoted as RBS-1 and RBS-2. These traces correspond respectively to the convolution results of code-1 and code-2 with the impulse response function of the fiber channel. When external perturbation occurs, the phases of the impulse response functions

* Corresponding author (email: znwang@uestc.edu.cn)

corresponding to the two sets of codes, denoted as $h_1(t)$ and $h_2(t)$, are subject to change. The phase difference results of $h_1(t)$ and $h_2(t)$ are shown in Figure A1. For code-1, the expected phase shift in its impulse response function $h_1(t)$ occurs within the disturbed region, as indicated by marker ②. However, concurrently, the impulse response function $h_2(t)$ corresponding to code-2 also exhibits a phase shift, indicated by marker ①. As a result, the perturbation information within RBS-2 maps to a specific region in RBS-1. This unintended crosstalk results in a false alarm on the code-1 channel, an issue known as ICC.

The RBS signal received by the detector is a composite signal resulting from the addition of RBS-1 and RBS-2 vectors. In the channel of code-1, the inherent RBS signal is expressed as the convolution of $h_1(t)$ and the auto-correlation function of code-1, denoted as $\overrightarrow{R_a}$. The mapped signal originating from code-2 is represented as the convolution of $h_2(t)$ with the cross-correlation functions of the two code sets, denoted as $\overrightarrow{R_c}$. The principle of ICC can be elucidated through the schematic enclosed within the red dashed box in Figure A1, where $\gamma$ signifies the original phase angle between $\overrightarrow{R_a}$ and $\overrightarrow{R_c}$. When the mapped signal from RBS-2 to RBS-1 contains perturbation information, the phase of $\overrightarrow{R_c}$ will change by $\Delta\varphi$. Consequently, even if there is no actual disturbance in that region on RBS-1, the phase of the demodulated RBS signal on the code-1 channel will transition from $\varphi_1$ to $\varphi_2$. This generates a phase difference of $\varphi_1 - \varphi_2$, representing the crosstalk, which cannot be eliminated through a phase differential process. Therefore, the phase of ICC from code-2 to code-1 is $\varphi_1 - \varphi_2$ and can be expressed as [3]:

$$\varphi_{\text{ ICC}} = 2\arctan\left(\frac{\left|\overrightarrow{R_c}\right|\sin\frac{\Delta\varphi}{2}}{\left|\overrightarrow{R_a}\right| - \left|\overrightarrow{R_c}\right|\cos\frac{\Delta\varphi}{2}}\right)\cos\left(\gamma + \frac{\Delta\varphi}{2}\right), \tag{A1}$$

where $\arctan(\cdot)$ is the inverse tangent operation. According to Eq. (A1), increasing the ratio of $\mid \overrightarrow{R_a} \mid / \mid \overrightarrow{R_c} \mid$ can effectively reduce crosstalk. In our proposed scheme, the magnitudes of $\mid \overrightarrow{R_a} \mid$ and $\mid \overrightarrow{R_c} \mid$ are directly proportional to the values of the peak sidelobe level (PSL) and peak cross-correlation level (PCCL) of the correlation functions between orthogonal codes. A higher PSL indicates a larger $\mid \overrightarrow{R_a} \mid$, while a smaller PCCL indicates a smaller $\mid \overrightarrow{R_c} \mid$. Therefore, in our work, adjusting the parameter of the mismatched filtering (MMF) allows us to fine-tune the difference between PSL and PCCL, thereby increasing the ratio of $\mid \overrightarrow{R_a} \mid / \mid \overrightarrow{R_c} \mid$. This strategic adjustment, as opposed to using mismatched filters without tuning $w$, results in more efficient ICC elimination.

## Appendix B Simulation results and analysis of CCM-DAS

To assess the feasibility of implementing co-channel multiplexed DAS (CCM-DAS), the performance of the proposed scheme is investigated and verified by simulation in MATLAB. The simulation process and results provide invaluable guidance for the experiment.

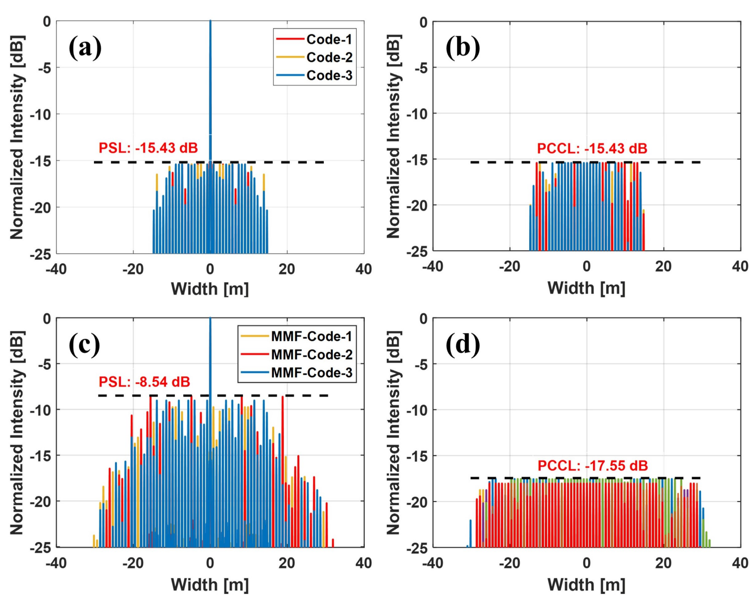


**Figure B1** The auto-correlation and cross-correlation functions for different decoding schemes. (a) Autocorrelation function and (b) cross-correlation of the matched filtering decoding. (c) Autocorrelation function and (d) cross-correlation of the mismatched filtering decoding.

In the CCM scheme with $M$ sets of orthogonal codes, three decisive parameters should be taken into account: the coding length $N$, the decoding length $L$, and single-pulse duration $T_{\rm d}$. Longer $N$ and $L$ ensure a low sidelobe level, while these three parameters and $M$ collectively correlate to the auto-correlation energy and the cross-correlation energy, which are determined by $(N+L)\cdot T_{\rm d}$ and $(M-1)\cdot(N+L)\cdot T_{\rm d}$, respectively. If the energy of cross-correlation is too high, ICC will be severe. Therefore, these parameters must be set appropriately. Here, when employing MF for decoding, $L=N$; whereas for MMF, $L=P$. In this scheme, a single chirp pulse with a width of 8 $ns$ and a bandwidth of 1 GHz is utilized as the phase-carrier. Then, 3 sets of orthogonal polyphase codes are generated, each has a 20-bit length, i.e. the duration of each code is 160 $ns$. Figures B1(a) and B1(b) demonstrate the PSL and PCCL obtained by MF decoding. In Figure B1(a), the auto-correlation functions of these three codes are displayed, where code-i represents the $i^{\rm th}$ code's auto-correlation; while Figure B1(b) illustrates the cross-correlation functions. The PSL and PCCL of MF decoding are both -15.43 dB here.

To achieve sufficiently low PCCL while ensuring that PSL meets the sensing requirement and does not compromise the spatial resolution, the length of the mismatched filter is set to 60-bit. Concurrently, the parameter $w$ is tuned to control the desired difference between PSL and PCCL, thereby further regulating ICC. In this case, $w$ is set to -9 dB. Solving the convex optimization problem stated in Eq. (11) in the manuscript yields 3 sets of corresponding mismatched filters. Figures B1(c) and B1(d) depict the maximum PSL and PCCL obtained by MMF decoding, where there is a 9 dB difference exists between PSL and PCCL, causing a higher ratio of $|\overrightarrow{R_a}|/|\overrightarrow{R_c}|$ than MF decoding, thereby further mitigating ICC. After decoding with MMF, the width of the decoded pulse can be restored to a single-bit pulse width of 8 $ns$. Although the spatial resolution of the system can be restored to the resolution corresponding to an 8 $ns$ chirp pulse at this stage, the presence of interference fading will affect the precise demodulation of disturbance signals. Therefore, after MMF decoding, fading elimination is needed. Here we apply the sub-chirp-pulse extraction algorithm (SPEA) [4], which will degrade the spatial resolution, manifested in the widening of the full width at half maximum (FWHM) of the auto-correlation functions, as shown by the solid lines in Figure B2, with an FWHM of 4.4 m.

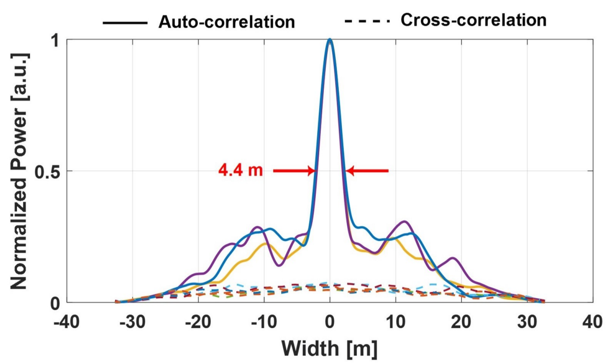


**Figure B2** The theory correlation function after MMF decoding and fading elimination (Simulation).

In the simulation, we model the RBS signal by convolving coded probing pulses with the impulse response function of the FUT. The impulse response function of an SMF conforms to a Rayleigh distribution regarding its envelope, and its phase adheres to a uniform distribution within the range of $[-\pi,\pi]$. External perturbations induce variations in the phase of the impulse response function. A 3 kHz sinusoidal disturbance is set at the end of 1 km sensing fiber. The interval between two adjacent codes is set to 4 $\mu s$, resulting in a code probe pulse repetition period of 12 $\mu s$, slightly greater than the round-trip time (RTT) of the probe pulse in the FUT. To ensure the quality of the demodulated signal, the gauge length (GL) is set to be larger than the theoretical spatial resolution of 4.4 m shown in Figure B2, which is 7.5 m. Consequently, the actual spatial resolution achieved in the simulation is 7.5 m. During the decoding process, both MF and MMF schemes are used. Other than the decoding method, all other demodulation processes are identical between the two schemes. Figure B3(a) demonstrates the time-distance domain map of the differential phase demodulated by MF. Apart from the disturbance signal at the end of the FUT, false disturbance signals are present at approximately 200 m and 600 m. They are the overlapping parts of traces from other codes with one of the codes, i.e., ICC. The areas where false disturbance signals occur can be represented as:

$$Z_{\rm ICC}^{i}=Z_{\Delta\varphi}-\frac{i}{2nM}\cdot cT_{\rm rep}, \tag{B1}$$

where $Z_{\Delta\varphi}$ is the region from the start of the disturbed position to the end of the FUT, where the phase of impulse response function is shifted by the disturbance. And $Z_{\rm ICC}^{i}$ represents the area of ICC present in $i^{\rm th}$ code's trace, with $0\leqslant Z_{\rm ICC}^{i}\leqslant L_{\rm FUT}$, where $L_{\rm FUT}$ is the fiber length.

The time-distance domain map decoded using MMF is shown in Figure B3(b), indicating little ICC in this depiction and 7.5 m spatial resolution. Furthermore, if the disturbance signal is weak, the false disturbance signals will be submerged in noise, which is acceptable in practical applications. Figure B3(c) displays the sinusoidal waveform of the demodulated disturbance signal, while Figure B3(d) shows its power spectral density (PSD). The PSD reveals harmonics at approximately 80.2 kHz and 86.2 kHz, a consequence of channel interlacing from different codes, which will appear at $1/T_{\rm rep}\pm f_{\rm dis}$, with $f_{\rm dis}$ representing the disturbance frequency. This is a common issue in channel multiplexing DAS. Nevertheless, the signal-to-noise (SNR) of the disturbance signal still reaches 28 dB. Additionally, the maximum value of the PSD's abscissa is 125 kHz, three times the maximum detectable frequency of the traditional single-pulse scheme, i.e., $1/2T_{\rm rep}$, implying an increase in response bandwidth. So far, the simulation results have provided preliminary validation of the proposed approach's feasibility.

Please refer to Appendix D for the phases and amplitudes of the three sets of orthogonal polyphase codes generated, along with their corresponding mismatched filters.

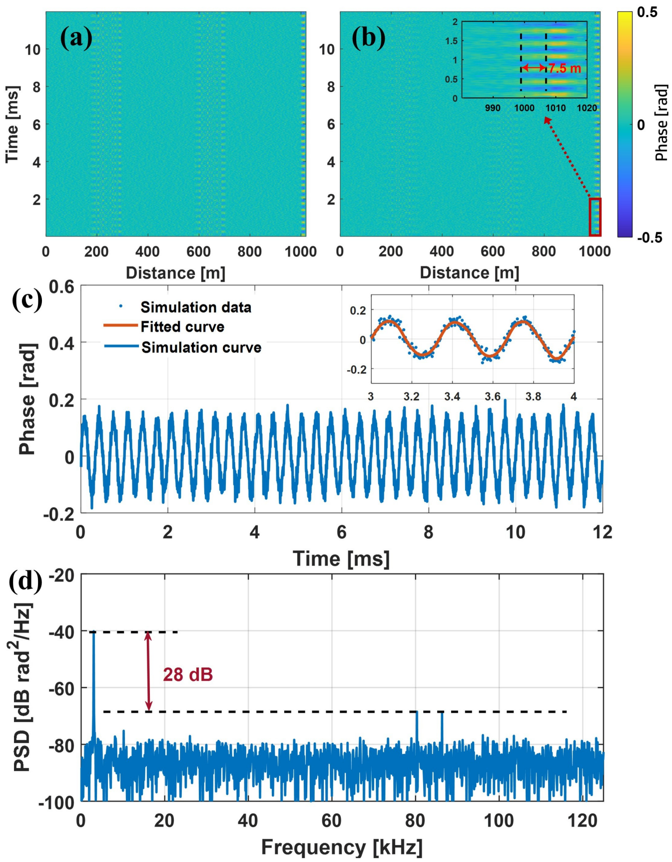


**Figure B3** Simulation results. (a) Time-distance domain map of the differential phase demodulated by matched filtering and (b) mismatched filtering. (c) Time-domain waveform of the demodulated 3 kHz sinusoidal signal. (d) The PSD of the demodulated signal.

## Appendix C Coding gain analysis in the proposed scheme

In optical-pulse-coding-based DAS (OPC-DAS), the coding gain is a pivotal metric, denoting the degree of the system's SNR enhancement. In this scheme, $M$ sets of orthogonal polyphase codes, each with a length of $N$ bits and a bit width of $T_{\mathrm{d}}$, modulate probe pulse into a coded pulse sequence with a repetition period of $T_{\mathrm{rep}}$. These codes are then decoded with MMF. As depicted in Eqs. (5) and (6) of the manuscript, when the PCCL and PSL of the cross-correlation functions meet the requirements, the scattered light from the coded pulse sequence can be restored to a single-pulse scattered light with a width of $T_{\mathrm{d}}$. Hence, in the ideal case, the response of the orthogonal codes can be construed as the discrete convolution of the codes and the single-pulse response, denoting the single-pulse response within the DAS system as $I_0(t)$. Considering the noise introduced during the processing of the RBS trace corresponding to the $i^{\mathrm{th}}$ code as $e_i(t)$, then the response generated independently by each $i^{\mathrm{th}}$ code can be represented as:

$$I_{\text{code-}i} = C_i * I_0(t) + e_i(t) \quad i = 1, 2, \ldots, M, \tag{C1}$$

where $C_i$ represents the $i^{\mathrm{th}}$ code sequence. After decoding with the corresponding mismatched filter, the resulting single-pulse response of the system can be expressed as:

$$\hat{I}_{\text{code-}i} = \frac{I_{\text{code-}i} \otimes D_i}{P} = I_0(t) + \frac{e_i(t) \otimes D_i}{P}, \quad i = 1, 2, \ldots, M, \tag{C2}$$

where $D_i$ represents the decoder for the $i^{\mathrm{th}}$ code, i.e., a mismatch filter of length $P$. As the decoder only affects the decoding process itself and not the actual signal power, Eq. (C2) can be rewritten as:

$$\hat{I}_{\text{code-}i} = I_0(t) + \frac{e_i(t) \otimes C_i}{N}, \quad i = 1, 2, ..., M. \tag{C3}$$

Assuming $e_i(t)$ represents uncorrelated additive Gaussian white noise with zero mean and variance $\delta^2$, the calculated mean square error (MSE) of the $i^{\rm th}$ decoded subsystem can be calculated as:

$$E\left\{\left[\hat{I}_{\text{code-}i}(t)-I_0(t)\right]^2\right\}=\frac{\delta^2}{N}. \tag{C4}$$

Subsequently, the results from $M$ sets of orthogonal codes are interweaved to achieve channel multiplexing, equating to $M$ independent samplings of a single event. This results in an $M$-fold increase in response bandwidth. At this stage, the signal power is maintained, while the noise variance is decreased to $1/M$ of its original value. Then the MSE of the proposed system can be expressed as:

$$E\left\{\left[\hat{I}(t)-I_0(t)\right]^2\right\}=\frac{\delta^2}{M\cdot N}. \tag{C5}$$

Compared with the MSE in the case of the traditional single-pulse scheme, the coding gain of CCM-DAS is calculated as:

$$G=\sqrt{\delta^2/\frac{\delta^2}{M\cdot N}}=\sqrt{M\cdot N}. \tag{C6}$$

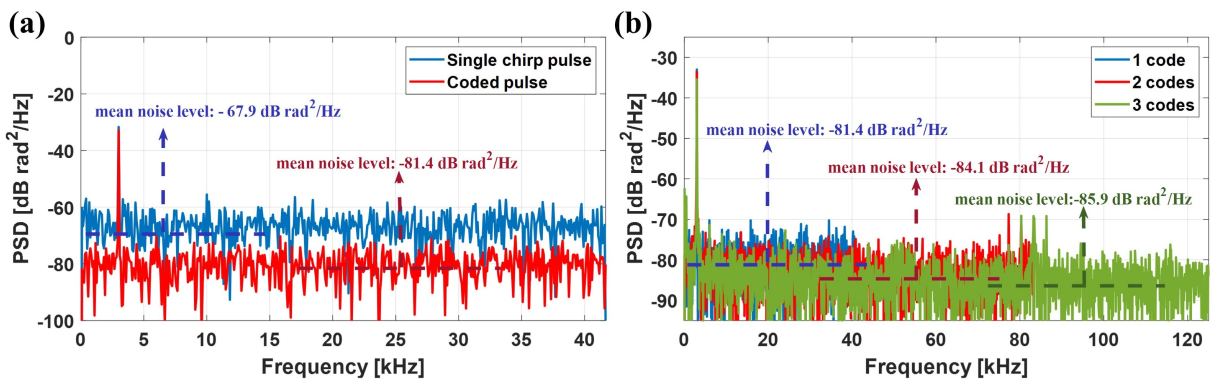


**Figure C1** (a) Mean noise levels of single chirp pulse and single-coded pulse sequence scheme (1 set of orthogonal code). (b) Mean noise levels of coded pulse sequence schemes with 1 set, 2 sets, and 3 sets of orthogonal codes.

Experiments are conducted to validate the accuracy of Eq. (C6), with the experimental setup aligned with that shown in Figure 3 of the manuscript. Initially, an 8 $ns$ chirp signal is used as the probe pulse in the single-pulse scheme, with a 3 kHz sinusoidal disturbance applied to the PZT. The PSD of the disturbance signal detected by this scheme is depicted as the blue curve in Figure C1(a). Subsequently, a 20-bit orthogonal coded pulse, each bit with a duration of 8 $ns$, serves as the probe pulse and is decoded using a 60-bit mismatched filter. The demodulation process is consistent with the single-pulse scheme, and the resulting PSD curve is represented as the red curve in Figure C1(a). The mean noise level of the single-coded scheme is found to be 13.5 dB lower than that of the single-pulse scheme, closely approximating the theoretical value of $20\log_{10}(\sqrt{20})$, which is 13 dB. Further experimentation involves replacing the probe pulse with coded pulse sequences generated by two and three sets of codes, each with a length of 20-bit. The resulting PSDs are shown as the red and green curves in Figure C1(b), respectively, with the single-coded scheme's PSD indicated by the blue curve. Theoretically, the mean noise level of the two-coded scheme should be 3 dB lower than that of the single-coded scheme, which corresponds to $20\log_{10}(\sqrt{2})$. Likewise, the mean noise level of the three-coded scheme should be 4.8 dB lower, corresponding to $20\log_{10}(\sqrt{3})$. The experimental results presented in Figure C1(b) closely match the theoretical predictions, thereby substantiating the coding gain of the proposed scheme.

## Appendix D Generated orthogonal codes and corresponding mismatched filters

In this scheme, the orthogonal polyphase codes are non-return-to-zero codes with uniform amplitude and phase varying between 0 and $2\pi$. Correspondingly, the mismatched filters are non-return-to-zero codes with random amplitude and phase varying between $-\pi$ and $\pi$. Additionally, the length $P$ of each mismatched filter exceeds the length $N$ of the orthogonal code. Figure D1 illustrates the phases of the orthogonal codes used in the experiments of this study and the amplitudes and phases of the corresponding mismatched filters. Note that $M$ represents the number of code groups. The values shown in Figure D1(a-f) are detailed in Tables D1- D6, respectively.

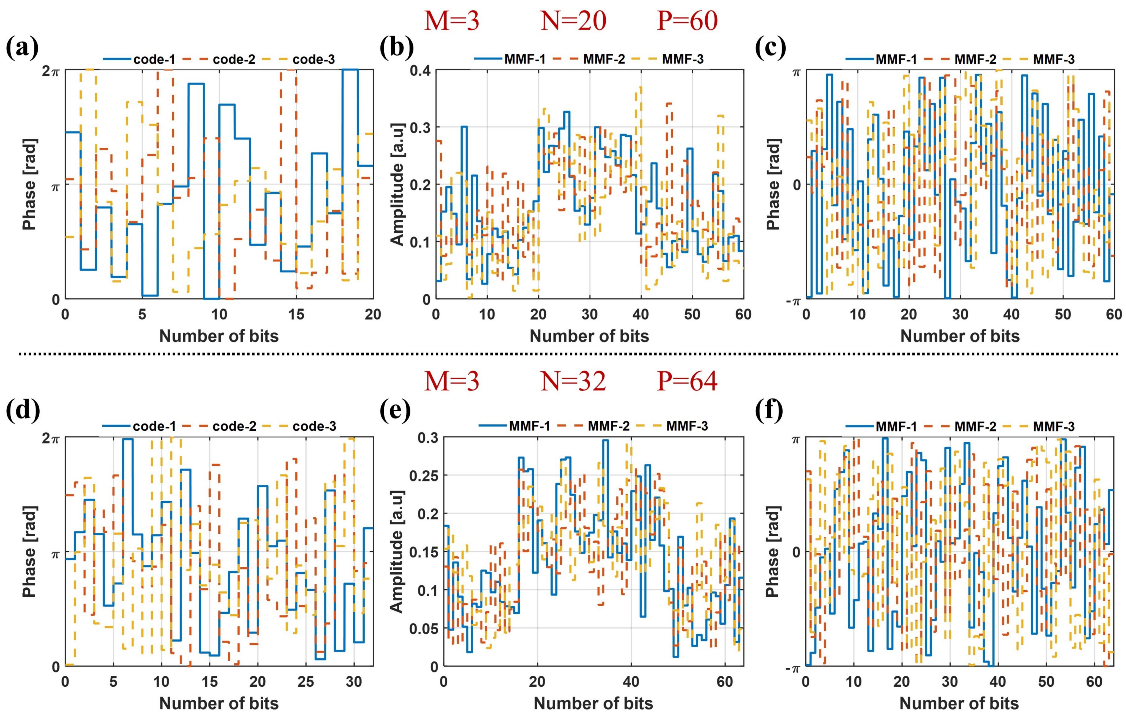


**Figure D1** Phases and amplitudes of the orthogonal codes and mismatched filters used in the experiments. (a) Phases of the 3 sets of 20-bit orthogonal codes and the normalized amplitudes (b) and phases (c) of their corresponding 60-bit mismatched filters. (d) Phases of the 3 sets of 32-bit orthogonal codes and the normalized amplitudes (e) and phases (f) of their corresponding 64-bit mismatched filters.

**Table D1** The phases of the generated 3 sets of 20-bit orthogonal polyphase codes.

| **No.** | **Phases** | | | | |
|---|---|---|---|---|---|
| Code-1 | 4.563 | 2.045 | 5.894 | 1.480 | 3.985 |
| | 0.795 | 0.087 | 0.000 | 2.903 | 2.344 |
| | 2.504 | 2.601 | 5.322 | 0.752 | 6.283 |
| | 0.599 | 3.078 | 4.392 | 1.433 | 3.645 |
| Code-2 | 3.278 | 2.104 | 3.311 | 2.443 | 0.714 |
| | 1.355 | 3.941 | 4.399 | 1.049 | 2.406 |
| | 4.105 | 6.283 | 0.000 | 6.283 | 0.690 |
| | 2.952 | 2.767 | 1.638 | 0.290 | 3.311 |
| Code-3 | 1.694 | 5.393 | 1.389 | 3.582 | 2.120 |
| | 6.283 | 4.768 | 1.770 | 2.936 | 3.549 |
| | 2.655 | 2.580 | 2.573 | 1.506 | 0.506 |
| | 0.479 | 0.190 | 3.229 | 0.703 | 4.521 |

**Table D2** The amplitudes of the generated 3 sets of 60-bit mismatched filters.

| No. | Amplitudes | | | | |
|---|---|---|---|---|---|
| MMF-1 | 0.031 | 0.108 | 0.297 | 0.286 | 0.081 |
| | 0.152 | 0.117 | 0.326 | 0.284 | 0.262 |
| | 0.195 | 0.054 | 0.213 | 0.216 | 0.118 |
| | 0.148 | 0.043 | 0.154 | 0.114 | 0.078 |
| | 0.095 | 0.103 | 0.162 | 0.130 | 0.065 |
| | 0.300 | 0.124 | 0.129 | 0.170 | 0.091 |
| | 0.034 | 0.152 | 0.176 | 0.236 | 0.218 |
| | 0.215 | 0.170 | 0.299 | 0.158 | 0.188 |
| | 0.135 | 0.298 | 0.262 | 0.078 | 0.066 |
| | 0.026 | 0.221 | 0.247 | 0.055 | 0.107 |
| | 0.078 | 0.267 | 0.258 | 0.101 | 0.110 |
| | 0.122 | 0.266 | 0.233 | 0.104 | 0.083 |
| MMF-2 | 0.275 | 0.033 | 0.155 | 0.186 | 0.241 |
| | 0.075 | 0.219 | 0.248 | 0.213 | 0.163 |
| | 0.111 | 0.134 | 0.214 | 0.279 | 0.176 |
| | 0.091 | 0.088 | 0.182 | 0.250 | 0.162 |
| | 0.139 | 0.207 | 0.282 | 0.055 | 0.121 |
| | 0.140 | 0.073 | 0.179 | 0.091 | 0.104 |
| | 0.077 | 0.153 | 0.154 | 0.074 | 0.221 |
| | 0.105 | 0.032 | 0.283 | 0.131 | 0.052 |
| | 0.154 | 0.263 | 0.301 | 0.112 | 0.057 |
| | 0.111 | 0.252 | 0.183 | 0.341 | 0.082 |
| | 0.231 | 0.236 | 0.223 | 0.114 | 0.140 |
| | 0.078 | 0.288 | 0.232 | 0.085 | 0.135 |
| MMF-3 | 0.110 | 0.067 | 0.182 | 0.203 | 0.086 |
| | 0.033 | 0.118 | 0.269 | 0.240 | 0.121 |
| | 0.061 | 0.063 | 0.236 | 0.189 | 0.142 |
| | 0.218 | 0.014 | 0.286 | 0.369 | 0.119 |
| | 0.220 | 0.157 | 0.098 | 0.195 | 0.036 |
| | 0.205 | 0.108 | 0.204 | 0.017 | 0.138 |
| | 0.002 | 0.152 | 0.283 | 0.025 | 0.096 |
| | 0.112 | 0.014 | 0.110 | 0.033 | 0.319 |
| | 0.035 | 0.315 | 0.177 | 0.209 | 0.031 |
| | 0.122 | 0.332 | 0.209 | 0.101 | 0.113 |
| | 0.151 | 0.255 | 0.288 | 0.057 | 0.066 |
| | 0.045 | 0.237 | 0.246 | 0.135 | 0.053 |

**Table D3** The phases of the generated 3 sets of 60-bit mismatched filters.

| No. | Phases | | | | |
|---|---|---|---|---|---|
| MMF-1 | -3.091 | 1.227 | 2.200 | -1.888 | 1.216 |
| | 0.909 | 1.903 | -0.290 | 1.974 | -2.328 |
| | -2.995 | 0.148 | 2.917 | -0.590 | 0.907 |
| | 0.959 | -2.778 | -3.124 | -2.626 | -2.514 |
| | 3.002 | -1.481 | 0.134 | -3.106 | -1.029 |
| | -0.577 | -3.089 | -0.479 | -0.384 | 1.766 |
| | 2.257 | -0.872 | -0.666 | 2.981 | -1.092 |
| | -1.509 | 1.441 | -2.108 | 0.365 | 2.474 |
| | 1.509 | -1.524 | 1.127 | 2.488 | -0.769 |
| | -1.809 | 1.034 | 2.994 | -0.315 | 1.308 |
| | 0.077 | 2.921 | 0.562 | 2.197 | -2.660 |
| | -2.986 | 0.382 | 1.654 | -0.821 | -0.276 |
| MMF-2 | 0.739 | -1.004 | 2.058 | 0.780 | -1.865 |
| | -0.235 | -1.739 | -2.556 | 2.558 | -0.556 |
| | 2.298 | -0.497 | 0.422 | 0.413 | 0.693 |
| | 0.477 | -1.541 | 2.982 | -2.864 | 2.760 |
| | 0.973 | 2.071 | 2.984 | 0.349 | -0.979 |
| | 0.143 | -1.603 | -1.670 | -1.250 | -0.701 |
| | -2.289 | -2.331 | -0.299 | 1.406 | 0.473 |
| | 2.847 | 1.001 | 1.165 | -1.619 | -2.251 |
| | -0.428 | -2.783 | 2.692 | -2.100 | -2.081 |
| | -0.165 | 1.444 | 1.030 | -0.204 | 0.383 |
| | -1.108 | -2.265 | -0.140 | 1.304 | 2.539 |
| | -1.189 | 2.909 | 0.631 | -0.723 | -1.966 |
| MMF-3 | 1.748 | 2.248 | -1.189 | 2.322 | 1.341 |
| | 1.121 | 0.160 | -1.680 | 3.133 | 0.396 |
| | 2.073 | -2.290 | 2.658 | 0.944 | -0.620 |
| | -0.323 | 1.690 | 0.564 | -1.569 | 3.027 |
| | -3.015 | 1.593 | 0.677 | -2.754 | 2.058 |
| | 0.693 | -0.928 | 2.392 | 0.701 | -1.070 |
| | 0.208 | -2.325 | 2.307 | -0.256 | -2.400 |
| | -0.012 | 2.971 | 3.079 | -2.993 | -2.578 |
| | -2.755 | 1.356 | -2.291 | 2.567 | -0.152 |
| | -0.189 | -0.132 | 2.973 | 1.364 | -0.865 |
| | -2.304 | 2.471 | 1.605 | -2.587 | -1.590 |
| | -2.999 | 1.000 | 0.225 | -2.241 | 2.245 |

**Table D4** The phases of the generated 3 sets of 32-bit orthogonal polyphase codes.

| No. | Phases | | | | | | | |
|---|---|---|---|---|---|---|---|---|
| Code-1 | 2.934 | 1.659 | 2.739 | 5.382 | 1.461 | 4.933 | 2.551 | 0.419 |
| | 3.670 | 2.265 | 3.586 | 3.101 | 2.578 | 3.284 | 2.090 | 2.257 |
| | 4.558 | 6.220 | 4.498 | 0.371 | 4.041 | 3.437 | 0.190 | 0.652 |
| | 3.619 | 3.608 | 0.702 | 0.292 | 0.918 | 1.546 | 4.813 | 3.779 |
| Code-2 | 4.684 | 3.678 | 2.157 | 0.000 | 0.667 | 4.314 | 1.646 | 5.249 |
| | 5.035 | 5.224 | 2.727 | 4.387 | 0.051 | 1.815 | 4.054 | 4.528 |
| | 1.406 | 2.959 | 3.871 | 2.108 | 2.684 | 1.365 | 0.393 | 2.609 |
| | 4.304 | 2.875 | 0.356 | 5.515 | 0.605 | 5.679 | 1.170 | 2.826 |
| Code-3 | 0.040 | 1.071 | 0.350 | 2.634 | 2.019 | 3.466 | 2.759 | 3.292 |
| | 3.125 | 3.630 | 6.169 | 3.890 | 1.395 | 2.396 | 1.397 | 6.232 |
| | 5.158 | 0.479 | 0.446 | 2.213 | 3.924 | 5.227 | 2.043 | 1.450 |
| | 1.169 | 3.222 | 6.271 | 2.780 | 3.999 | 0.907 | 5.053 | 2.398 |

**Table D5** The amplitudes of the generated 3 sets of 64-bit mismatched filters.

| No. | Amplitudes | | | | | | | |
|---|---|---|---|---|---|---|---|---|
| MMF-1 | 0.184 | 0.125 | 0.273 | 0.238 | 0.198 | 0.229 | 0.101 | 0.061 |
| | 0.048 | 0.122 | 0.255 | 0.270 | 0.191 | 0.248 | 0.012 | 0.096 |
| | 0.136 | 0.097 | 0.258 | 0.273 | 0.296 | 0.065 | 0.169 | 0.091 |
| | 0.091 | 0.110 | 0.122 | 0.224 | 0.142 | 0.263 | 0.079 | 0.056 |
| | 0.052 | 0.084 | 0.191 | 0.176 | 0.176 | 0.165 | 0.102 | 0.106 |
| | 0.018 | 0.078 | 0.161 | 0.148 | 0.148 | 0.221 | 0.026 | 0.193 |
| | 0.082 | 0.077 | 0.130 | 0.171 | 0.160 | 0.158 | 0.041 | 0.032 |
| | 0.078 | 0.069 | 0.094 | 0.175 | 0.139 | 0.098 | 0.034 | 0.116 |
| MMF-2 | 0.130 | 0.031 | 0.257 | 0.121 | 0.163 | 0.264 | 0.083 | 0.075 |
| | 0.029 | 0.071 | 0.150 | 0.180 | 0.080 | 0.191 | 0.027 | 0.022 |
| | 0.142 | 0.160 | 0.208 | 0.212 | 0.154 | 0.240 | 0.155 | 0.070 |
| | 0.028 | 0.047 | 0.213 | 0.243 | 0.176 | 0.226 | 0.047 | 0.171 |
| | 0.081 | 0.161 | 0.177 | 0.172 | 0.193 | 0.172 | 0.059 | 0.086 |
| | 0.057 | 0.045 | 0.160 | 0.251 | 0.231 | 0.251 | 0.135 | 0.147 |
| | 0.087 | 0.074 | 0.129 | 0.181 | 0.094 | 0.230 | 0.106 | 0.159 |
| | 0.072 | 0.084 | 0.166 | 0.123 | 0.243 | 0.179 | 0.137 | 0.052 |
| MMF-3 | 0.154 | 0.096 | 0.191 | 0.151 | 0.142 | 0.248 | 0.079 | 0.054 |
| | 0.179 | 0.024 | 0.181 | 0.267 | 0.266 | 0.121 | 0.073 | 0.155 |
| | 0.123 | 0.037 | 0.235 | 0.201 | 0.184 | 0.181 | 0.048 | 0.185 |
| | 0.084 | 0.053 | 0.216 | 0.113 | 0.176 | 0.124 | 0.092 | 0.111 |
| | 0.158 | 0.104 | 0.209 | 0.146 | 0.117 | 0.202 | 0.034 | 0.116 |
| | 0.118 | 0.044 | 0.140 | 0.180 | 0.181 | 0.192 | 0.095 | 0.190 |
| | 0.054 | 0.132 | 0.168 | 0.159 | 0.209 | 0.233 | 0.213 | 0.021 |
| | 0.072 | 0.133 | 0.200 | 0.136 | 0.291 | 0.213 | 0.091 | 0.049 |

**Table D6** The phases of the generated 3 sets of 64-bit mismatched filters.

| No. | Phases | | | | | | | |
|---|---|---|---|---|---|---|---|---|
| MMF-1 | -3.108 | 2.773 | 3.096 | 2.499 | 1.849 | 2.340 | 1.212 | 2.297 |
| | -2.775 | -2.087 | -2.669 | -2.846 | 2.970 | 2.578 | -1.020 | 2.868 |
| | -1.537 | -1.335 | -1.645 | -1.879 | -2.084 | 0.372 | -2.305 | -2.379 |
| | -0.163 | 0.217 | -2.058 | 0.279 | -0.047 | -1.097 | -0.861 | -1.639 |
| | 0.074 | 0.267 | 1.514 | -0.282 | -0.567 | 0.377 | -0.538 | 0.749 |
| | -1.701 | -2.723 | 2.178 | 2.837 | -3.018 | 1.940 | 3.073 | 1.140 |
| | 1.710 | 1.041 | 0.144 | 0.225 | -3.141 | 0.134 | 1.063 | 0.203 |
| | 2.175 | 0.616 | 2.698 | 0.358 | 1.048 | -2.253 | -0.987 | 1.684 |
| MMF-2 | 2.197 | 2.584 | -1.671 | 1.352 | -0.309 | 1.818 | -1.085 | 2.886 |
| | -2.341 | 0.103 | -0.851 | 2.203 | 0.601 | -2.281 | -2.211 | -0.467 |
| | -0.072 | 3.110 | 1.446 | -2.199 | 2.666 | -0.111 | 1.702 | 1.148 |
| | -3.063 | 0.409 | -1.992 | 0.569 | 0.421 | 1.643 | -0.330 | -2.267 |
| | 0.834 | 0.402 | -2.741 | 0.514 | -2.279 | -1.261 | -0.876 | -0.138 |
| | -1.048 | -2.103 | -0.612 | -1.769 | 1.840 | -1.086 | 2.442 | 1.171 |
| | -1.274 | 0.842 | 2.971 | 1.838 | 0.894 | 2.514 | -0.741 | -3.141 |
| | 2.423 | 1.912 | -3.006 | -0.803 | -0.757 | 2.840 | 0.296 | -0.074 |
| MMF-3 | 1.976 | 2.892 | 0.135 | -0.285 | 1.236 | 2.537 | 2.944 | -1.738 |
| | -2.213 | -0.508 | 2.680 | 0.207 | 1.349 | 1.804 | 2.763 | -2.670 |
| | 0.336 | -0.656 | -0.854 | 0.862 | -3.118 | 2.045 | 2.437 | -1.669 |
| | 3.023 | -0.684 | 1.036 | 0.236 | -2.325 | -1.550 | -2.880 | 0.071 |
| | -1.411 | -0.610 | 1.761 | 2.274 | -2.671 | -2.686 | 3.067 | 1.969 |
| | 0.385 | 1.433 | -2.620 | -2.446 | 2.430 | 0.197 | 1.830 | -2.509 |
| | 2.114 | 2.474 | 0.471 | 2.157 | -1.239 | 1.928 | 2.740 | -0.204 |
| | -0.036 | -2.044 | -3.109 | 2.735 | 0.732 | 2.458 | -2.638 | -2.759 |

**References**


1 Chen D, Liu Q W, Fan X Y, et al. Distributed fiber-optic acoustic sensor with enhanced response bandwidth and high signal-to-noise ratio. J Lightwave Technol, 2017, 35: 2037–2043
2 Wu M S, Fan X Y, Zhang X P, et al. Frequency response enhancement of phase-sensitive OTDR for interrogating weak reflector array by using OFDM and vernier effect. J Lightwave Technol, 2020, 38: 4874–4882
3 Deng Y P, Liu Q W, Liu S T, et al. Multipath quasi-distributed acoustic sensing based on space division multiplexing and time-gated OFDR. IEEE Sensors J, 2023, 23: 11615–11620
4 Xiong J, Wang Z N, Wu Y, et al. Single-Shot COTDR using sub-chirped-pulse extraction algorithm for distributed strain sensing. J Lightwave Technol, 2020, 38: 2028–2036